LAWRENCE
LIVERMORE
NATIONAL
LABORATORY

Dynamic Dislocation Mechanisms for the Anomalous Slip in a Single-Crystal BCC Metal Oriented for "Single Slip"

L. Hsiung

January 12, 2007

DYNAMIC DISLOCATION MECHANISMS FOR THE ANOMALOUS SLIP IN A SINGLE-CRYSTAL BCC METAL ORIENTED FOR "SINGLE SLIP"

Luke L. Hsiung

Materials Science and Technology Division
Chemistry, Materials, and Life Sciences Directorate

Objectives and accomplishments

Dislocation substructures of high-purity Mo single crystals deformed under uniaxial compression at room temperature to an axial strain of 0.6 % were investigated in order to elucidate the underlying mechanisms for the $\{0\bar{1}1\}$ anomalous slip in bcc metals [1], which is also known as the violation of Schmid law [2]. The test sample was oriented with the stress axis parallel to a nominal "single-slip" orientation of $[\bar{2}\ 9\ 20]$, in which $(\bar{1}01)\ [111]$ is the primary slip system that has a maximum Schmid factor (m = 0.5), which requires the lowest stress to operate among the twelve $\{\bar{1}10\}$ <111> slip systems. Nevertheless, the recorded stress-strain curve reveals no easy-glide or single-slip stage; work hardening starts immediately after yielding. Moreover, the result of slip trace analysis indicates the occurrence of anomalous slip on both the (011) and $(0\bar{1}1)$ planes, which according to the Schmid law requires relatively higher stresses to operate. TEM examinations of dislocation structures formed on the $(\bar{1}01)$ primary slip plane reveal that in addition to the $(\bar{1}01)\ [111]$ slip system, the coplanar $(\bar{1}01)\ [1\bar{1}1]$ slip system which has a much smaller Schmid factor (m = 0.167) is also operative. Similarly, $(0\bar{1}1)\ [111]$ (m = 0.25) is cooperative with the coplanar $(0\bar{1}1)$ $[\bar{1}11]$ slip system (m = 0.287) on the $(0\bar{1}1)$ slip plane, and (011) $[1\bar{1}1]$ (m = 0.222) is cooperative with the coplanar (011) $[11\bar{1}]$ slip system (m = 0.32) on the (011) plane. The occurrence of $\{0\bar{1}1\}$ anomalous slip is accordingly proposed to be originated from the cooperative dislocation motion of the $\pm\frac{1}{2}[111]$ and $\pm\frac{1}{2}[1\bar{1}1]$ dislocations on the $(\bar{1}01)$ slip plane; the mutual interaction and blocking of $\pm\frac{1}{2}[111]$ and $\pm\frac{1}{2}[1\bar{1}1]$ dislocations not only cause an increase of glide resistance to the dislocation motion on the $(\bar{1}01)$ plane but

also render the ±½[111] and ±½[1$\bar{1}$1] screw dislocations to cross slip and propagate from the ($\bar{1}$01) slip plane onto the (0$\bar{1}$1) and (011) intersecting slip planes. That is, the ±½[111] screw dislocations cross slip from (111) onto (0$\bar{1}$1), and the ±½[1$\bar{1}$1] screw dislocations cross slip from (111) onto (011), which subsequently render another two slip systems, (0$\bar{1}$1) [$\bar{1}$11] and (011) [11$\bar{1}$], to become operative. As a result, all ½<111>-type dislocations, i.e. all <111> slip, take part in the plastic deformation of the [$\bar{2}$ 9 20]-oriented single-crystal Mo.

Introduction

Computer simulations and empirical studies of the core structure of single dislocation in bcc metals over the last few decades have made enormous contributions to interpret many abnormal mechanical behaviors of bcc metals: tension/compression stress asymmetry, high Peierls (friction) stress for the motion of screw dislocations, and strong strain-rate and temperature dependence of yield and flow stresses [3]. However, the single-dislocation core model remains inconclusive to elucidate a peculiar anomalous slip behavior of bcc metals, which occurs on planes for which the Schmid factors are fifth and sixth in the order of largest Schmid factors for the {110} <111> slip systems, and for which the resolved shear stress is less than half that on the ($\bar{1}$01) [111] primary system. Although numerous and intensive studies have been conducted for the last four decades since Duesbery [1] first reported the occurrence of anomalous slip in Nb single crystals in 1969, see reviews of the subject in the literature [4-9], the governing mechanisms remain elusive. Results of numerous studies have indicated that the anomalous slip in bcc metals in general occurs at low temperatures; it accompanies a high work-hardening rate and fine and planar slip traces, which are in contract to a low work-hardening rate in association with coarse and wavy slip traces as the anomalous slip becomes absent at elevated temperatures. Progress has been made recently on obtaining crucial evidences to rationalize the anomalous slip behavior of bcc metals through careful TEM observations of dislocation substructures evolved in the primary and anomalous slip planes of Mo single crystals that were oriented along a nominal "single-slip" orientation and were uniaxially tested at room temperature. It was found that

instead of being caused by the motion of single-dislocations, the anomalous slip can be attributed to the collective effects of dislocation multiplication, interaction, and propagation. The novel results are reported and discussed here in order to depict the underlying mechanisms that lead to the Schmid-law violation of the crystal plasticity in bcc metals. It is interesting to note that one major reason Mo single crystals were chosen for the current study is due to the fact that {110} <111> is the only predominant slip system at room temperature [10], which is different from other bcc metals such as Ta, Fe, and V, in which both {110} <111> and {112} <111> are the operative slip systems at room temperature.

Approach

Mo single crystals grown by a two-pass zone-refinement process were obtained from Accumet Materials Company, NY. The as-received crystals were then decarburized at 1800°C for 460 hours under an oxygen partial pressure of 2.1×10^{-6} Torr followed by a 24-hour bake at 2300°C under an ultrahigh vacuum (UHV) of 10^{-11} Torr. The residual resistivity ratio of the crystals was increased from 1890 to 4458 after the UHV-purification. The test sample used in this study has a square cross section that measures 5.5 mm on each side; the sample also has a length of 15 mm as illustrated in Figure 1a. Prior to the compression test, the test sample was heat treated at 1500°C for 1 hour, 1200°C for 1 hour, and 1000°C for 1 hour at a vacuum pressure of 8×10^{-11} Torr. Testing of single-crystal sample involves compressing the test sample between two platen surfaces under precise conditions. Details of the experimental design and test apparatus were described elsewhere [11]. To measure shear strain during compression, resistance-strain gage rosettes were attached to the sides of the test sample. These rosettes measured the biaxial strain on the sample surface during deformation. A compression test was conducted on a single-crystal sample oriented with a stress axis parallel to a nominal "singe-slip" orientation of $[\bar{2}\ 9\ 20]$, where the primary slip system, $(\bar{1}01)\ [111]$, is the only system that has a maximum Schmid factor (m = 0.5) as depicted in Figure 1b. Samples were then compressed to approximately 0.6 % axial strain at nominal strain rates of 10^{-3} s^{-1} and 1 s^{-1}. TEM foils were sliced from an as-annealed crystal and the gauge section of the tested sample with the foil precisely

sliced parallel to the ($\bar{1}$01), (0$\bar{1}$1), and (011) planes. The foils were subsequently perforated by a standard twin-jet electropolishing technique in a solution of 75 vol.% ethanol and 25 vol.% sulfuric acid at 25 V and -10°C. TEM examinations of deformation substructure were mainly conducted from the sample tested at 1 s^{-1}.
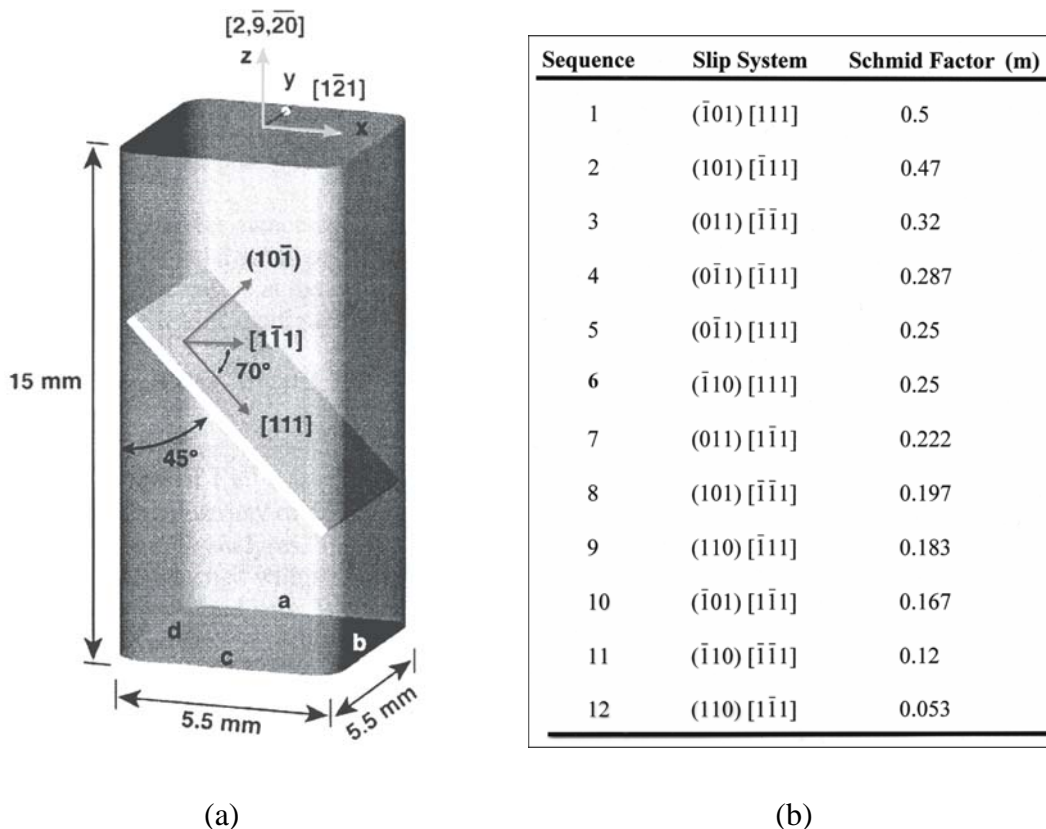

Sequence	Slip System	Schmid Factor (m)
1	($\bar{1}$01) [111]	0.5
2	(101) [$\bar{1}$11]	0.47
3	(011) [$\bar{1}\bar{1}$1]	0.32
4	(0$\bar{1}$1) [$\bar{1}$11]	0.287
5	(0$\bar{1}$1) [111]	0.25
6	($\bar{1}$10) [111]	0.25
7	(011) [1$\bar{1}$1]	0.222
8	(101) [$\bar{1}\bar{1}$1]	0.197
9	(110) [$\bar{1}$11]	0.183
10	($\bar{1}$01) [1$\bar{1}$1]	0.167
11	($\bar{1}$10) [$\bar{1}\bar{1}$1]	0.12
12	(110) [1$\bar{1}$1]	0.053

(a)   (b)

Fig. 1. (a) Geometry and dimensions of test sample [11]. The four faces of the sample are labeled as "A" through "D." The primary slip system, ($\bar{1}$01) [111], is also labeled. (b) A list of Schmid factors for the {011} <111> slip systems in the [$\bar{2}$ 9 20]-oriented test sample.

Result and Discussion

Stress-strain response and slip trace analysis

A stress-strain curve recorded from the uniaxial compression of a [$\bar{2}$ 9 20]–oriented sample and optical micrographs of slip traces observed from two adjacent faces of the tested sample are shown in Figures 2a and 2b, respectively. It can be readily seen from the stress-strain curve that work hardening takes place immediately after yielding; no single-slip or easy-glide stage is observed. The result of slip trace analysis

shown in Figure 2b clearly reveals the appearance of fine and planar ($\bar{1}01$) slip lines in association with localized ($0\bar{1}1$) and (011) slip bands on the tested sample. TEM images showing the slip traces of ($\bar{1}01$), (101), and (011) observed from a ($0\bar{1}1$)-sliced foil are displayed in Figure 3 together with the ($0\bar{1}1$) stereographic projection used for analyzing the slip traces.
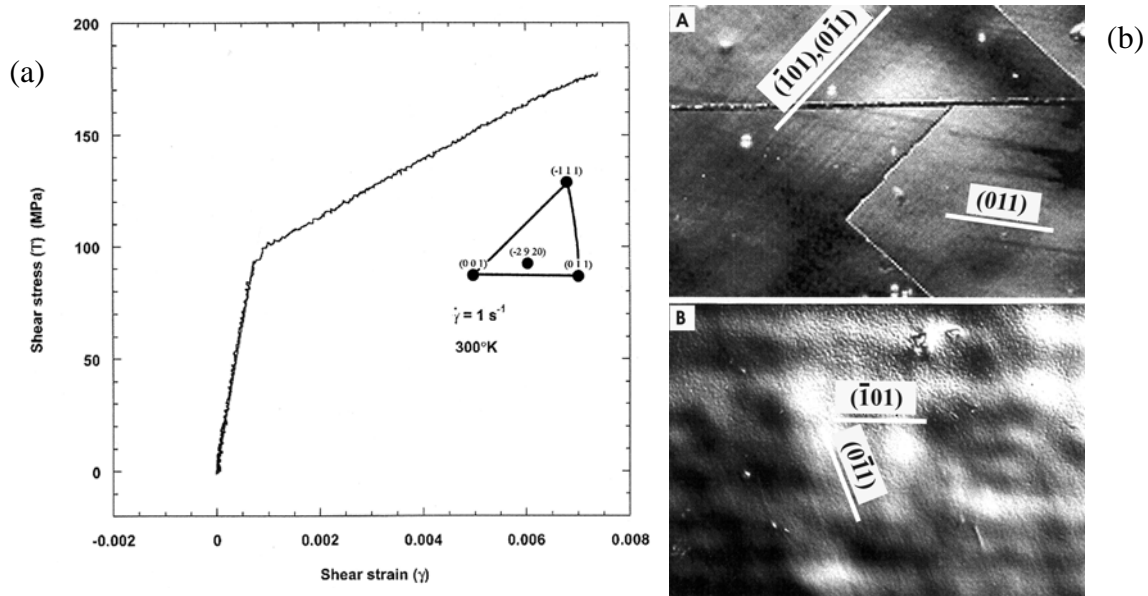

Fig. 2. (a) A stress-strain curve of the [$\bar{2}$ 9 20]–oriented crystal uniaxially compressed at room temperature at a strain rate of 1 s^{-1}. (b) Optical micrographs of slip traces observed from two adjacent faces of the tested sample showing the appearance of ($\bar{1}01$), ($0\bar{1}1$), and (011) slip lines.
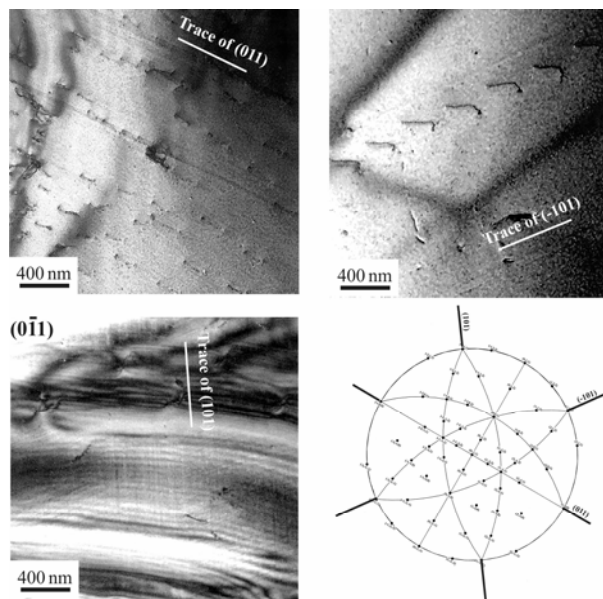

Fig. 3. Bright-field TEM images showing multiple slip traces observed from a ($0\bar{1}1$)-sliced foil; **FN** (foil normal) = [$0\bar{1}1$].

Initial dislocation structure in as-annealed crystals

Pre-existing dislocations in an as-annealed crystal observed from the ($\bar{1}$01)-, (0$\bar{1}$1)-, and (011)-sliced foils are shown in Figures 4a, 4b, and 4c, respectively. The dislocation density is estimated to be in the range of $10^6 \sim 10^7$ cm^{-2}. In general, as demonstrated in Figures 5a and 5b by **g** • **b** analyses, each dislocation line in the as-annealed crystal contains many "grown-in" kink/jog segments and is found to be near-screw in character. It is also suggested that each dislocation line in the as-annealed crystal, instead of solely lying on a single plane as it is commonly believed, is in fact threading across many different planes. In other words, the initial dislocations are in fact threading dislocations with numerous segments lying on different slip planes, which make a one-dimensional line defect to physically occupy a three-dimensional space in a bulk sample as illustrated in Figure 5c.
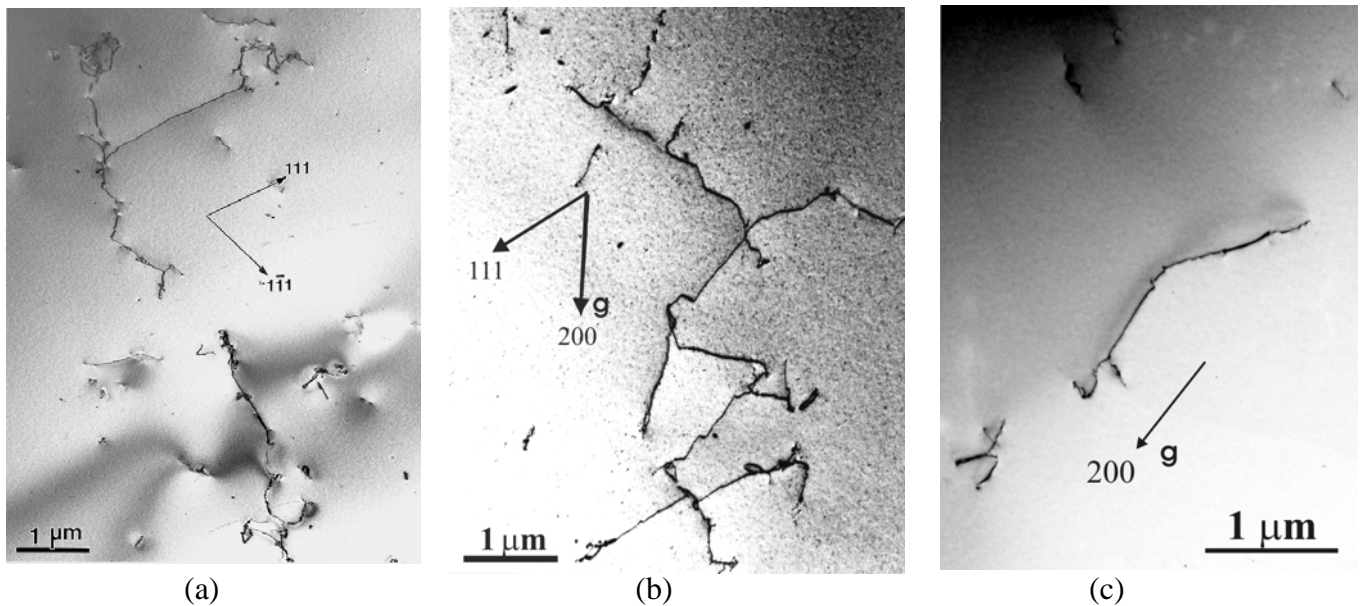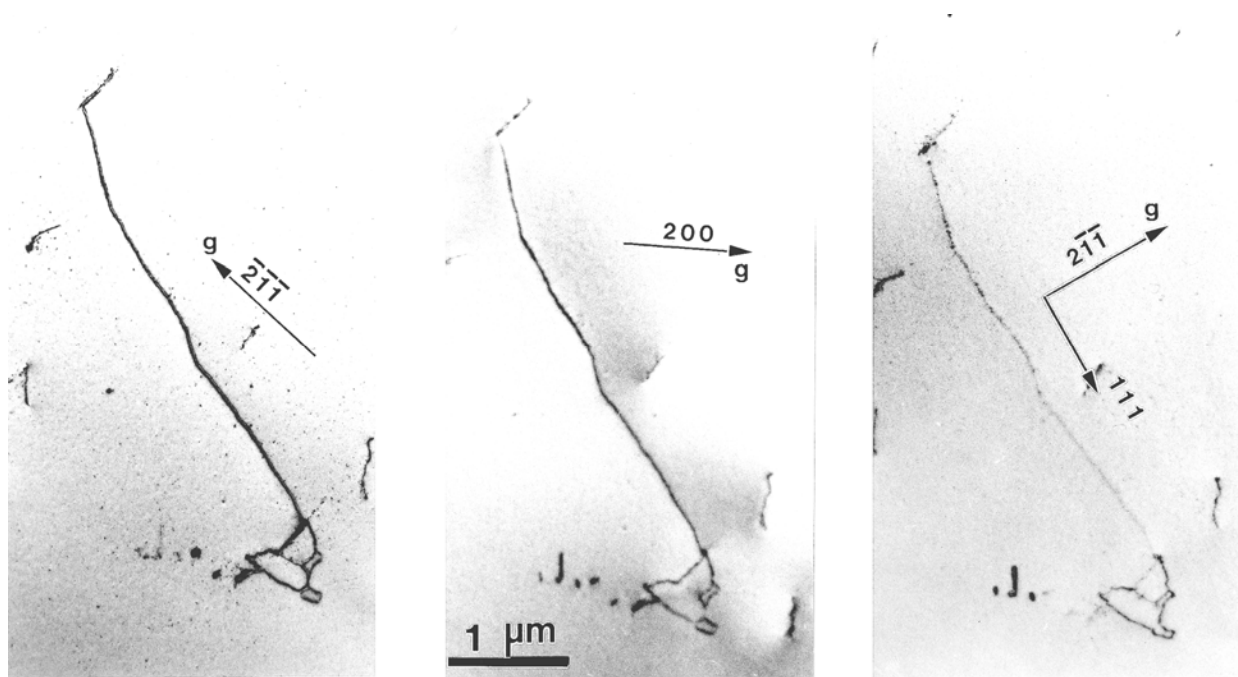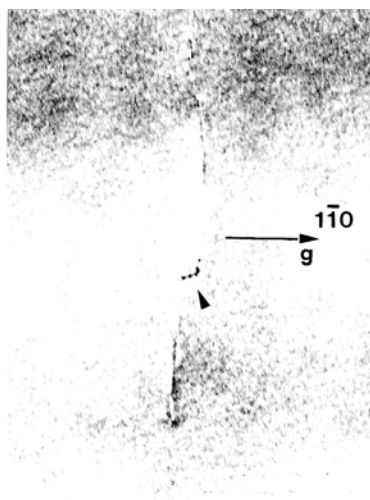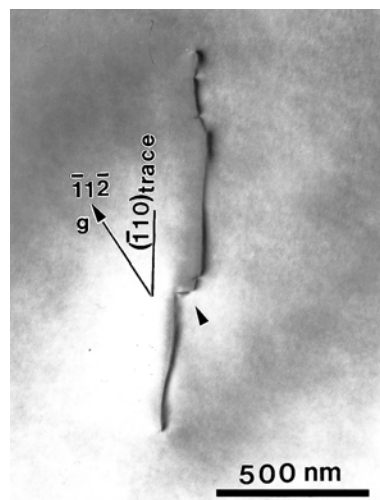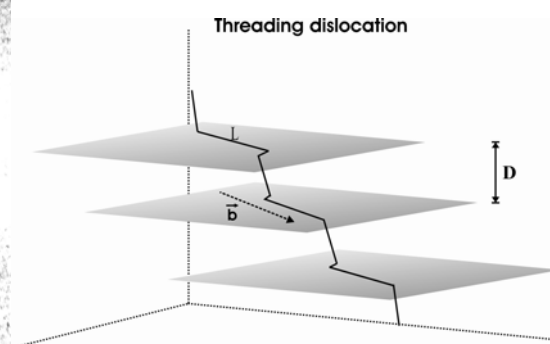

(a)   (b)   (c)

Fig. 4. Two-beam bright-field TEM images showing the pre-existing dislocations in an as-annealed crystal: (a) ($\bar{1}$01)-sliced foil, **Z** (zone axis) = [$\bar{1}$01], **g** = 020; (b) (0$\bar{1}$1)-sliced foil, **Z** = [0$\bar{1}$1], **g** = 211; (c) (011)-sliced foil, **Z** = [011], **g** = 200.

(a)

(b)   (c)

Fig. 5. (a) A $\mathbf{g} \cdot \mathbf{b}$ analysis for a near-screw dislocation ($\mathbf{b} = \pm\frac{1}{2}[111]$) in a $(0\bar{1}1)$-sliced foil; the contrast of a near-screw dislocation line becomes faint when $\mathbf{g} = 2\bar{1}\bar{1}$ and $\mathbf{g} \cdot \mathbf{b} = 0$. (b) A $\mathbf{g} \cdot \mathbf{b}$ analysis for a jogged screw dislocation ($\mathbf{b} = \pm\frac{1}{2}[111]$) viewed in the [110] direction. The line segment becomes invisible when $\mathbf{g}$ $= 1\bar{1}0$ and $\mathbf{g} \cdot \mathbf{b} = 0$ for a pure screw dislocation, yet the jog segment with an edge character (marked by an arrow) remains visible. (c) A schematic illustration of a threading (or jogged) dislocation line that physically occupies a three-dimensional space in a bulk sample.

Dynamic dislocation multiplication

Typical dislocation structures of samples tested at 10^{-3} s^{-1} and 1 s^{-1} are shown in Figure 6. The measured dislocation density increased by about two orders of magnitude to a range of $10^8 \sim 10^9$ cm^{-2}. In addition to long screw dislocations, many jogs and/or kinks (marked by arrows) were observed to form along the screw dislocations in the sample tested at 10^{-3} s^{-1} (Figure 6a). The average jog height and the free segments between jogs were found to increase significantly as compared to those observed in the as-annealed crystal. While little dislocation debris was found in the sample tested at 10^{-3} s^{-1}, much more dislocation debris and dipoles, presumably generated from the non-conservative motion of jogged screw dislocations, were observed in the sample tested at 1 s^{-1} (Figures 6b and 6c).
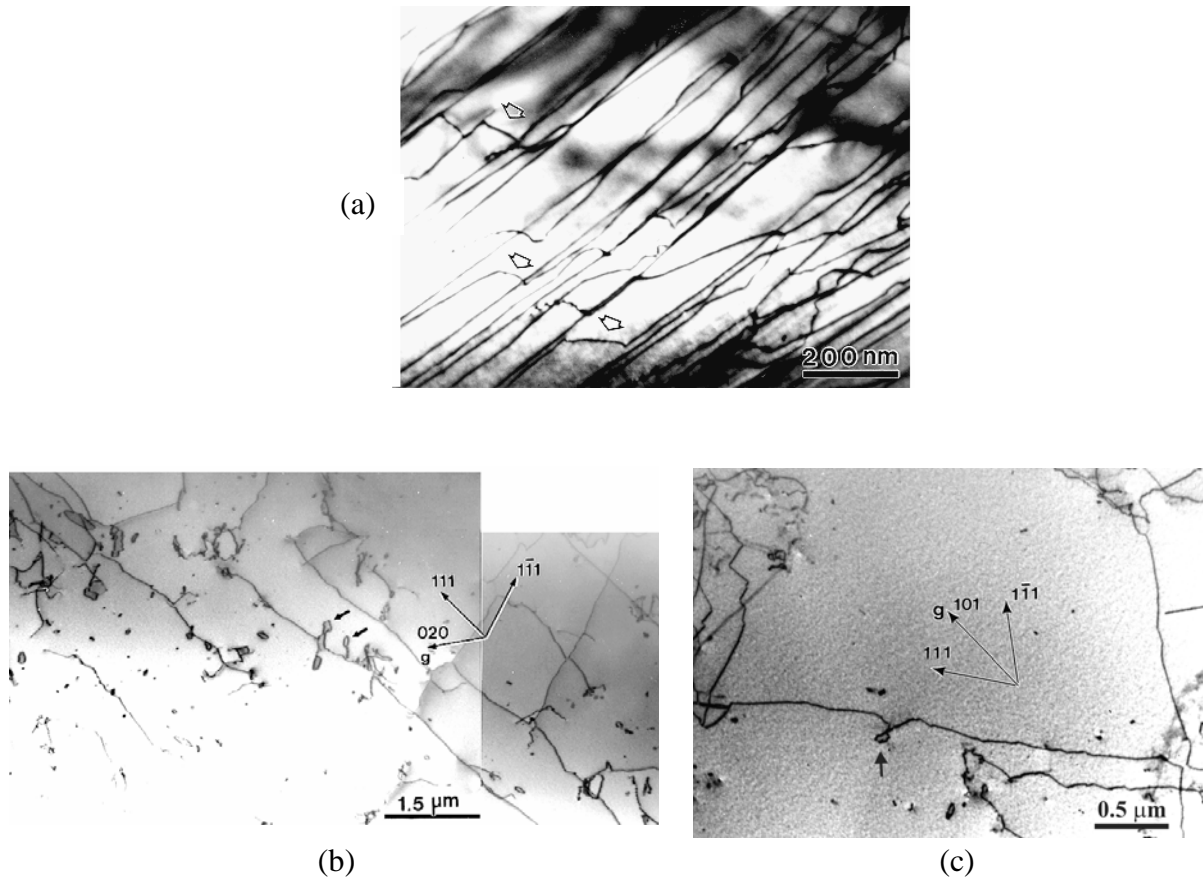

(a)

(b)   (c)

Fig. 6. (a) A bright-field TEM image showing long ±½[111] screw dislocation lines associated with large jogs (indicated by arrows) in the sample tested at 10^{-3} s^{-1}. (b, c) Bright-field TEM images showing the formation of dislocation dipoles and debris in the sample tested at 1 s^{-1}. Notice that dislocation dipoles (marked by arrows) were pinched off from a ±½[111] screw dislocation line.

Since jog segments can act as effective pinning obstacles for the motion of jogged screw dislocation, it is accordingly postulated that each segmented portion of a threading dislocation can multiply and interact with one another very differently under different loading conditions. According to the Frank-Read dislocation multiplication mechanism [12], dislocation can multiply by repeatedly bowing out a free segment of dislocation line lying in a slip plane, and the shear stress (τ) required to bow out a line segment (l) is given as: $\tau \approx \mu b/l$. Thus, there may exist a critical length ($l^* \approx \mu b/\tau_a$) of free segment for a given applied shear stress (τ_a). Any length of free segment l which is smaller than l^* will be permanently immobile, while any length of segment greater than l^* are potentially mobile. It is therefore suggested that a jogged or threading screw dislocation can act as either an obstacle to impede dislocation motion, which will be further discussed later, or dynamic sources for dislocation multiplication and dipole formation depending on loading conditions that are further elaborated below.

When deformed under quasi-static conditions, screw dislocation segments (pinned by jogs) bow out between the superjogs under an applied shear stress (τ) to a curvature, as shown in Figures 7a and 7b, yet they are still immobile since the initial length (l_o) of each free segment is smaller than the critical length (l^*). In addition to the force exerted on dislocation segments by the applied shear stress, each jog is subjected to a net force (F_x) parallel to the Burgers vector as a result of the bowing of unevenly spaced link segments between jogs under small strains, which is schematically illustrated in Figure 7c. The magnitude of net force can be expressed as:

$$F_x = \Gamma(\cos\phi_2 - \cos\phi_1),$$

where $\phi = \sigma b l/2\Gamma$, and Γ is the line tension. Applying Taylor expansion to $\cos\phi$, thus

$$F_x \approx \frac{b^2 \sigma^2}{8\Gamma}(l_1^2 - l_2^2).$$

The force causes large loop to grow at the expanse of neighboring short loops by drifting the jog at P. The jog drifting velocity (v_j) can be related to its mobility (D_j/kT) according to the Einstein mobility relation [13]:

$$v_j = \frac{D_j}{kT} F_x$$

where D_j is the jog diffusivity. That is, each jog in Figure 7b moves in such a direction so that the shorter segments become still shorter and the longer segments are expanded. The jogs of like-sign tend to coalesce in order to reduced line energy and result in the increase of jog height. Consequently, the stress-induced jog pile-up and coalescence renders an increase of both segment length and jog height; the jog coalescence continues until the segment length (l) and jog height (d) are greater than critical values (defined below) so that applied stress begins to push each line segment to precede multiple dislocation multiplication.

$$L > l^* \approx \mu b / \tau, \text{ and}$$

$$d > d_c \approx \mu b / 8\pi (1-v)\tau.$$

Here, a mutual attraction force between adjacent bowing edge segments of opposite signs can define d_c. That is, the originally immobile screw dislocations become multiple sources for dislocation multiplication as a result of the process of jog migration and coalescence.

When deformed under high strain-rate conditions, the nucleation and migration of double kinks on screw dislocations become more rapidly according to the following equation [10]:

$$v_k = \frac{\sigma b L D_k}{kT} \exp[-\frac{2W_k}{kT}]$$

where, v_k is the migration velocity of double kinks, L the length of free segment, D_k/kT the kink mobility, D_k the kink diffusivity, W_k the formation energy for double kinks, which is considered to be a function of stress, i.e. it decreases with increasing applied stress. Accordingly, the rapid increase of stress on a link segment causes the double-kinks to pile-up at the ends of the segment. This in turn causes the angle θ to increase rapidly to approach $90°$, which causes the net force on a jog to vanish and thus retards the migration and

coalescence of jogs. Under this circumstance, long jogs may still have sufficiently large jog-height to operate the "dynamic" sources. Jogs of small height, on the other hand, draw out dislocation dipoles, as illustrated in Figure 7e, in which the dipolar segments (marked by + and −) cannot by-pass one another as a result of a greater interaction force due to a small jog height. This leads to the formation of a tail of two edge dislocations with the same Burgers vector but of opposite sign, which is called a dislocation dipole.
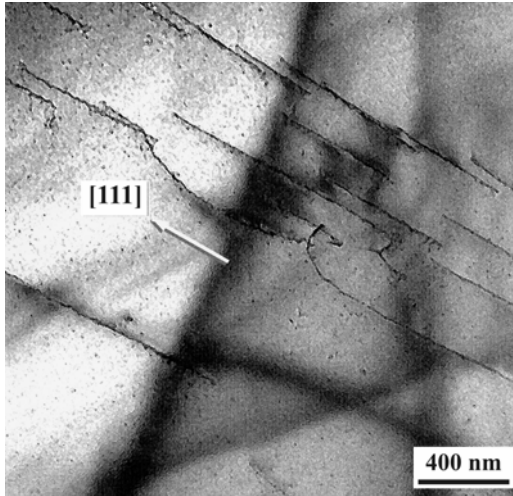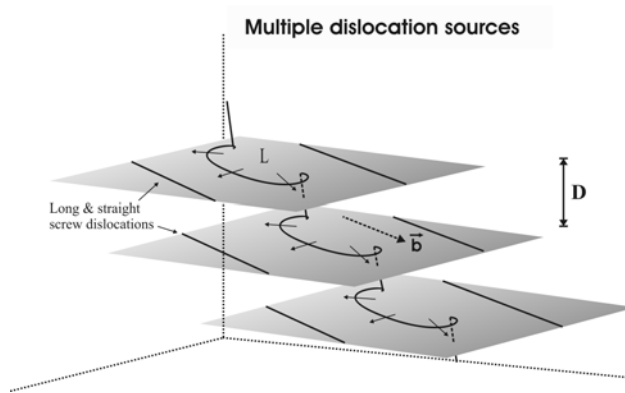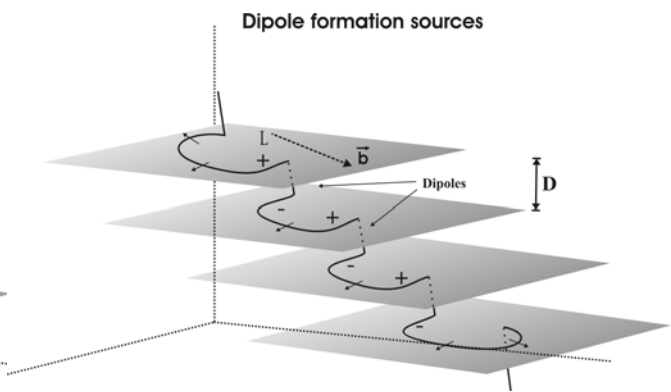

(a)
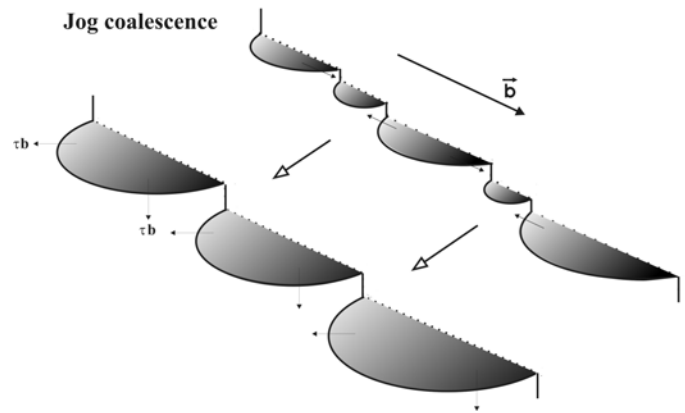
(b)
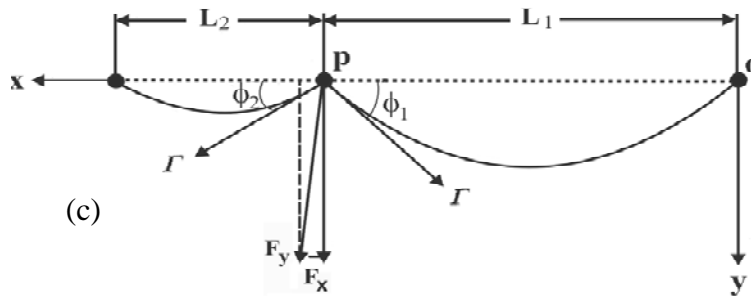
(c)

(d)

(e)

Fig. 7. (a) A typical TEM image showing the bowing of several dislocation segments in a tested sample. (b) A schematic illustration of dynamic dislocation sources generated from a jogged screw dislocation line through a jog coalescence process resulting from the unequal-length of free segments. (c) The resolved forces F_x and F_y acting on the jog (pinning point) resulting from the link segments of unequal lengths, L_1 and L_2, bowing under low strain. (d) A schematic illustration of multiple Frank-Read sources generated from a jogged screw dislocation with a large jog height. (e) A schematic illustration of dislocation dipole sources generated from a jogged screw dislocation with a small jog height.

Coplanar dislocation arrays and cooperative slip systems

Dislocation structures in the sample tested at 1 s^{-1} were carefully investigated from the foils sliced parallel to the ($\bar{1}$01), (0$\bar{1}$1), and (011) slip planes. In addition to the long screw dislocations and debris shown in Figures 6a and 6b, coplanar screw dislocation arrays were also found to form in these three planes studied, i.e., the ±½[111] and ±½[1$\bar{1}$1] screw dislocation arrays on the ($\bar{1}$01) plane (Figure 8a), the ±½[111] and ±½[$\bar{1}$11] screw dislocation arrays on the (0$\bar{1}$1) plane (Figure 8b), and ±½[1$\bar{1}$1] and ±½[11$\bar{1}$] screw dislocation arrays on the (011) plane (Figure 8c). These observations reveal that at least six slip systems, i.e., a pair of cooperative slip systems on each of the ($\bar{1}$01), (0$\bar{1}$1), and (011) planes as illustrated in Figure 9: ($\bar{1}$01) [111], ($\bar{1}$01) [1$\bar{1}$1], (0$\bar{1}$1) [111], (0$\bar{1}$1) [$\bar{1}$11], (011) [1$\bar{1}$1], and (011) [11$\bar{1}$], were operative in the early stages of plastic deformation of this "single-slip" oriented sample. As a result of the operation of these multiple slip systems, the actual translation direction of the bottom of the test sample measured by the laser sensors is shown in Figure 8a [11], which is matched fairly well with the predicted translation direction shown in Figure 8b based upon the combination of four operative slip directions: [111], [1$\bar{1}$1], [$\bar{1}$11], and [11$\bar{1}$] assuming a uniform crystal deformation. More investigations are needed in order to explain the discrepancy between the predicted and recorded translation directions. It is interesting to note that Schmid factor of the ($\bar{1}$01) [1$\bar{1}$1] slip system (m = 0.167) is only about one third that of the ($\bar{1}$01) [111] primary system (m = 0.5); the operation of such a slip system of the 10th sequence among the twelve (see Figure 1b)

obviously can not be explained by the Schmid law. It is accordingly suggested that the mechanisms for the anomalous slip are intimately related to the formation of coplanar dislocation arrays on the $(\bar{1}01)$, $(0\bar{1}1)$, and (011) slip planes. The underlying mechanisms for the anomalous slip in bcc metals can be unveiled if the mechanisms for the formation of coplanar dislocation arrays can be realized.
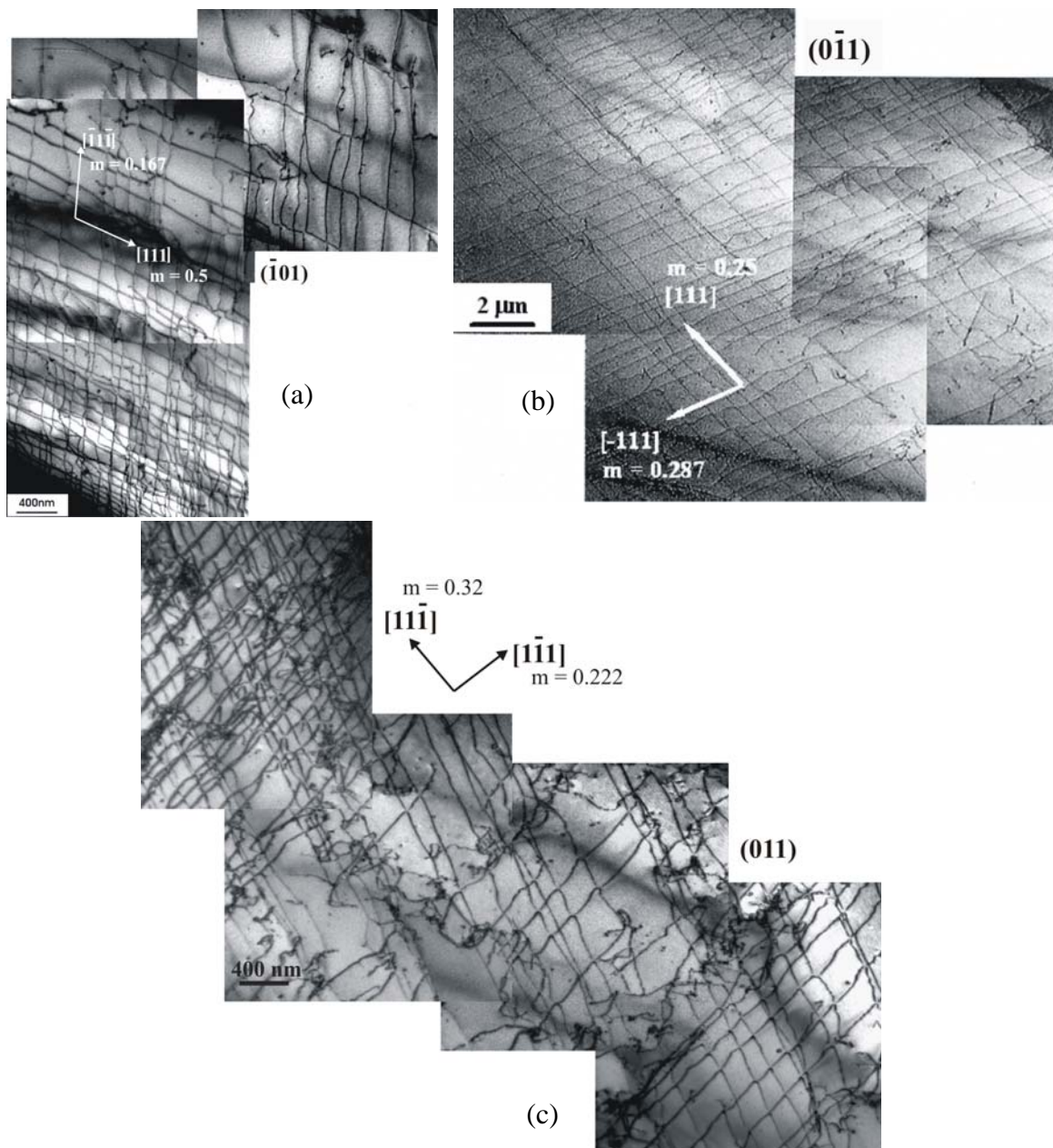

Fig. 8. Bright-field TEM images showing the formation of (a) the $\pm\frac{1}{2}[111]$ and $\pm\frac{1}{2}[1\bar{1}1]$ screw dislocation arrays on the $(\bar{1}01)$ plane, (b) the $\pm\frac{1}{2}[111]$ and $\pm\frac{1}{2}[\bar{1}11]$ screw dislocation arrays on the $(0\bar{1}1)$ plane, and (c) $\pm\frac{1}{2}[1\bar{1}1]$ and $\pm\frac{1}{2}[11\bar{1}]$ screw dislocation arrays on the (011) plane. Schmid factors (m) for each slip system are also specified.
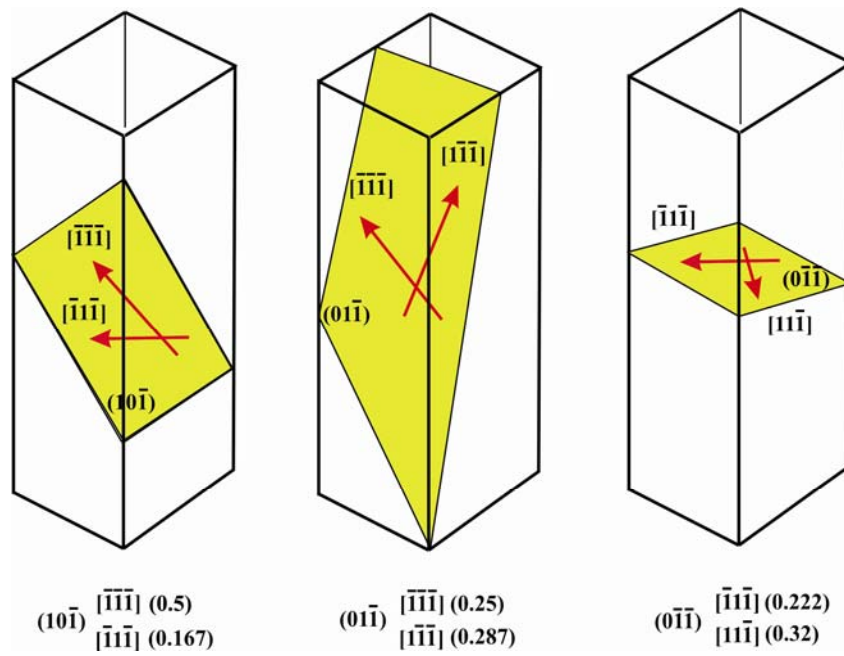
Fig. 9. Schematic illustrations of the cooperative slip systems in the $(10\bar{1})$, $(01\bar{1})$, and $(0\bar{1}\bar{1})$ slip planes.
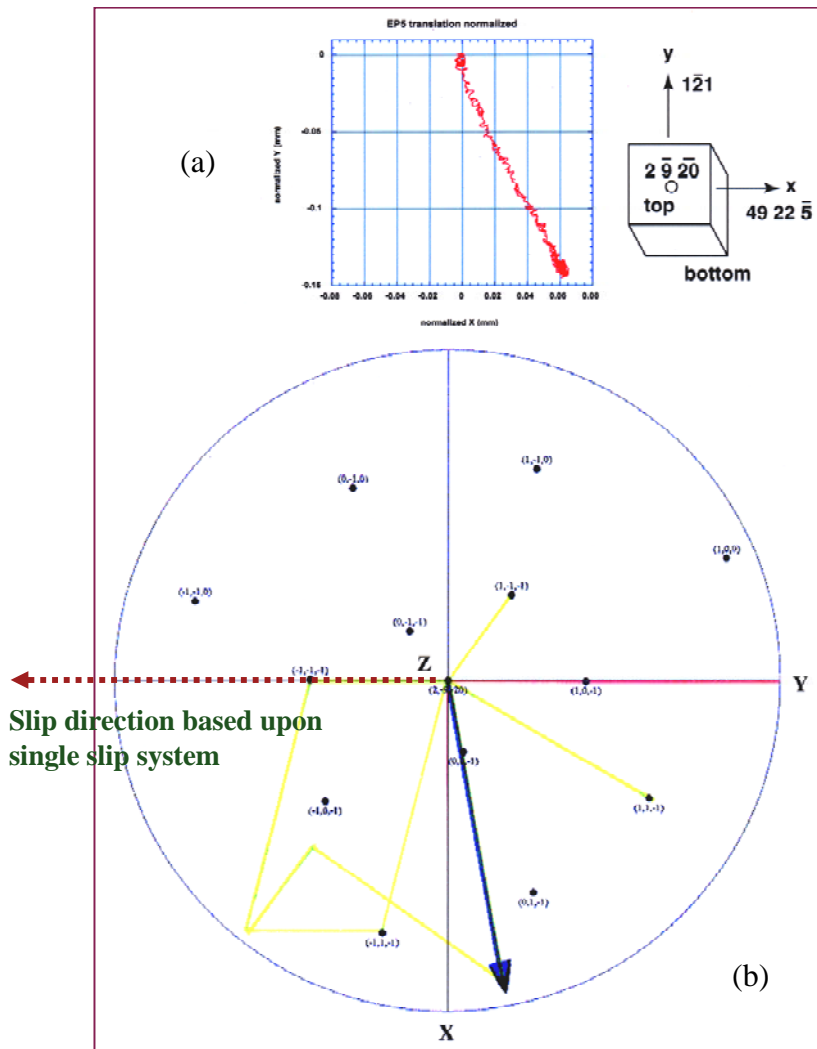

Fig. 10. (a) The translation direction of the bottom of the test sample measured by the laser sensors. The total linear translation was approximately 150 mm in a combination of the positive x and negative y directions [11]. (b) The predicted translation direction (marked by a blue arrow) based on the combination of four operative slip directions: [111], $[1\bar{1}1]$, $[\bar{1}11]$, and $[11\bar{1}]$ assuming a uniform crystal deformation. Sample translation direction based upon a single slip, i.e., $(\bar{1}01)$ [111], is also indicated by a red arrow.

Proposed mechanisms for the formation of coplanar dislocation arrays

It has been demonstrated in Figure 7 that the pre-existing screw dislocations associated with "grown-in" jogs can evolve from a self-pinning and immobile configuration into dynamic multiplication sources by a rate-dependent jog-coalescence process. Moreover, the self-pinning screw dislocations can also act as obstacles to impede dislocation motion, which are exemplified and elaborated in Figures 11a – 11c. Initially, only the $\pm\frac{1}{2}[111]$ dislocations can multiply and move on the $(\bar{1}01)$ plane; later, the motion of an array of $\pm\frac{1}{2}[111]$ dislocations are impeded and blocked at site **P** by a pre-existing $\pm\frac{1}{2}[1\bar{1}1]$ dislocation segment pinned at site **S** (Figure 11a). Although the applied force acting on the $\pm\frac{1}{2}[1\bar{1}1]$ dislocation is initially too low to overcome the glide resistance for bowing the pinned dislocation segment, the force may effectively increase with increasing interaction force between the impeded dislocation array and the pinned dislocation segment as a result of both an increasing number of dislocations added into the $\pm\frac{1}{2}[111]$ dislocation array and a closer distance between the dislocation array and the pinned dislocation segment. When the effective force eventually increases to exceed the glide resistance for the bowing and motion of the pinned dislocation segment, a $\pm\frac{1}{2}[1\bar{1}1]$ cooperative dislocation source is generated on the $(\bar{1}01)$ plane, as illustrated in Figure 11b. It is accordingly suggested that the simultaneous operations of the $\pm\frac{1}{2}[111]$ and the $\pm\frac{1}{2}[1\bar{1}1]$ dislocation sources on the $(\bar{1}01)$ primary slip plane, both originate from pre-existing screw dislocations, are responsible for the formation of the $\pm\frac{1}{2}[111]$ and $\pm\frac{1}{2}[1\bar{1}1]$ coplanar dislocation arrays as shown in Figures 8a and 11c.
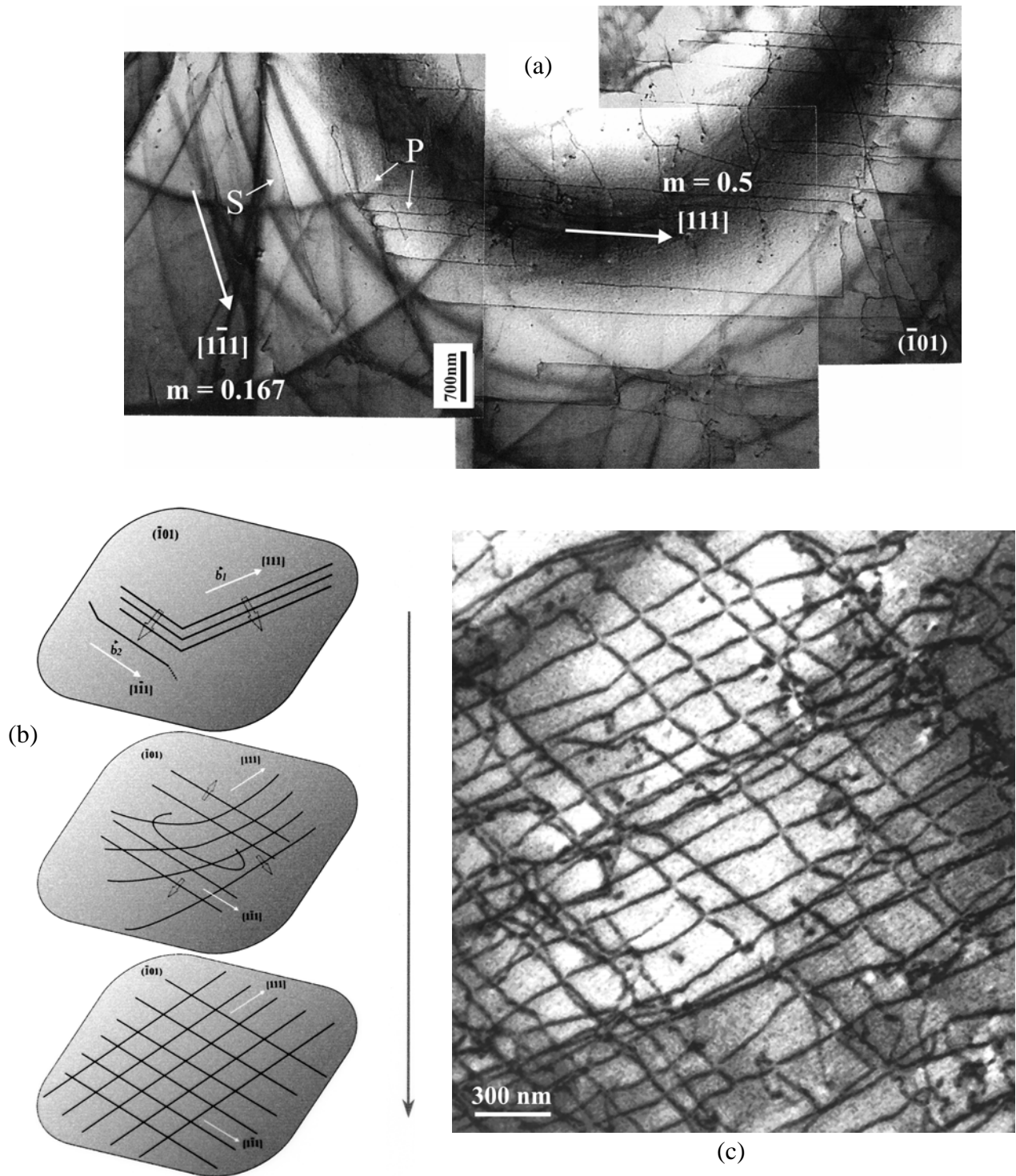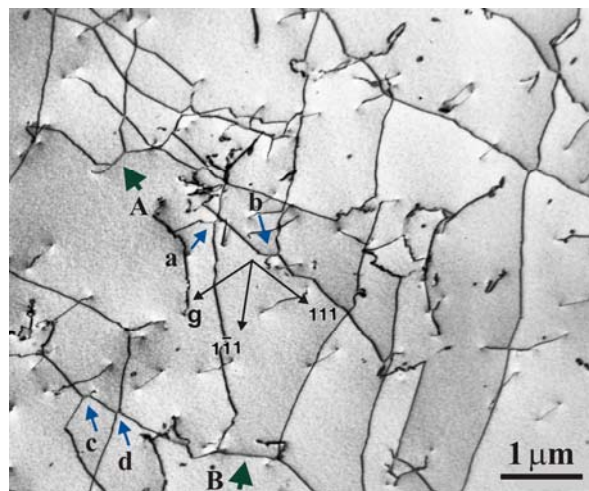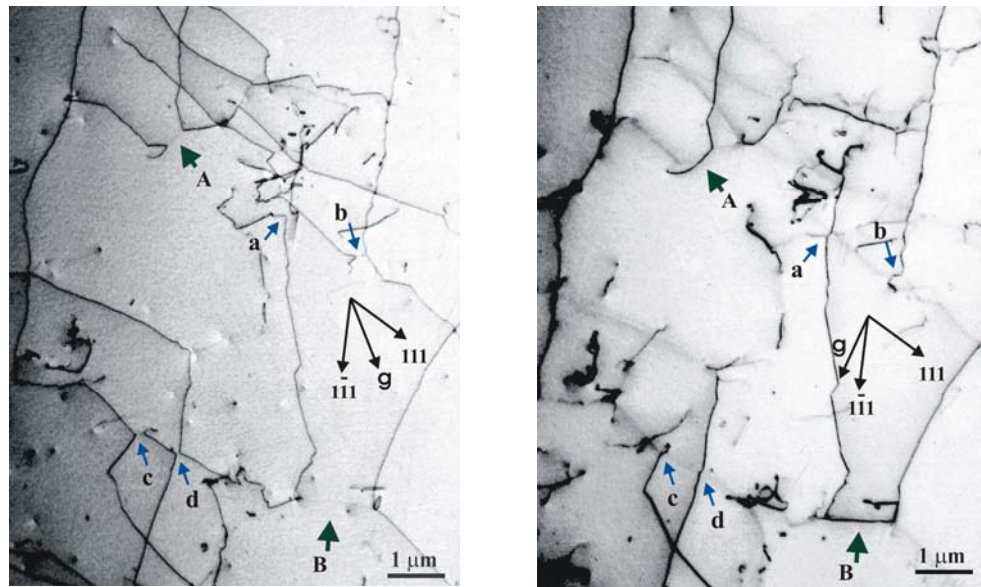
Fig. 11. (a) A bright-field TEM image showing the interaction between the ½[111] dislocation arrays (at site **P**) and pre-existing ½[1$\bar{1}$1] dislocation segment (at site **S**). (b) A schematic illustration of the operation of a ½[1$\bar{1}$1] cooperative dislocation source. (3) A bright-field TEM image showing typical coplanar dislocation arrays observed on the {$\bar{1}$01} slip plane.

Formation of the <010>-type junction dislocations

Unlike the mutual interception or cutting of dislocation lines that move on the different slip planes, the motion of ±½[111] and ±½[1$\bar{1}$1] coplanar dislocation arrays can result in not only trapping and blocking the dislocation arrays when moving on a single ($\bar{1}$01) plane, but also the generation of ±[010] junction dislocations by the reaction of ±½[111] ($\mathbf{b_1}$) + ±½[$\bar{1}$1$\bar{1}$] ($\mathbf{b_2}$) → ±[010] ($\mathbf{b_3}$), which is energetically feasible in accordance with the Frank energy criterion: $b_1^2 + b_2^2 > b_3^2$ [14], when moving on adjacent ($\bar{1}$01) planes. The results of $\mathbf{g} \cdot \mathbf{b}$ analyses to verify the formation of ± [010] junction dislocations are shown in Figures 12a – 12c. The ± [010] junction dislocations can be identified using the reflection vectors ($\mathbf{g}$) of ±[101], which are available in the [$\bar{1}$01]-zone electron diffraction pattern. The contrast of ±[010] junction dislocations, which are visible in both Figure 12a ($\mathbf{g} = 0\bar{2}0$) and Figure 12c ($\mathbf{g} = 1\bar{2}1$), becomes invisible in Figure 12b when $\mathbf{g} = 101$ and $\mathbf{g} \cdot \mathbf{b_3} = 0$. Likewise, the contrast of ±½[111] dislocations are visible in Figure 11a ($\mathbf{g} = 0\bar{2}0$) and Figure 11b ($\mathbf{g} = 101$) becomes invisible in Figure 12c ($\mathbf{g} = 1\bar{2}1$) when $\mathbf{g} \cdot \mathbf{b_1} = 0$. Meanwhile, the contrast of ±½[1$\bar{1}$1] dislocations remains visible in Figures 11a – 11c. Although no $\mathbf{g} \cdot \mathbf{b}$ experiment was carried out to verify the formation of the <100>-type junction dislocations on the (0$\bar{1}$1) and (011) planes, it is anticipated that similar reactions, ±½[$\bar{1}$$\bar{1}$1] + ±½[$\bar{1}1\bar{1}$] → ±[100] on the (011) plane and ±½[111] + ±½[1$\bar{1}$$\bar{1}$] → ±[100] on the (0$\bar{1}$1) plane, can also take place favorably.

(a)

(b)   (c)

Fig. 12. Two-beam bright-field TEM images obtained from the same specimen area showing the results of $\mathbf{g} \cdot \mathbf{b}$ analyses to verify the formation of the [010]-type junction dislocations in the $(\bar{1}01)$ plane, $\mathbf{Z} \approx [\bar{1}01]$; (a) $\mathbf{g} = 0\bar{2}0$, (b) $\mathbf{g} = 101$, (c) $\mathbf{g} = 1\bar{2}1$. Note that the small junction dislocations are labeled by lower-case letters (a, b, c, d), and the large junction dislocations are labeled by upper-case letters (A, B).

The mutual trapping and blocking of coplanar dislocation arrays and the formation of <100>-type junction dislocations can lead to not only the increase in glide resistance for dislocation motion but also the formation of dislocation pile-ups. Typical observations of the dynamic pile-ups of screw dislocations on the $(\bar{1}01)$ planes caused by either the formation of junction dislocations or the mutual trapping of coplanar dislocation arrays are shown in Figures 13a and 13b, respectively. It should be noted that since the cross slip of screw dislocations is a thermally activated process, observations of the pile-ups of screw dislocations indicate that at room temperature a single screw dislocation in Mo is in continuous motion and has no driving force for cross slipping so as to by-pass an obstacle, i.e., slip remains planar. This in fact can lead to more severe stress concentrations as a result of the formation of dislocation pile-ups. The cross-slip of screw dislocation can however take place when a stress concentration (σ^*) acting on the first screw

dislocation in a pile-up array of n screw dislocations under an applied stress (σ), i.e., $\sigma^* = n\sigma$ [15], exceeds a threshold stress for cross slip at zero temperature, i.e., stress-induced cross slip.
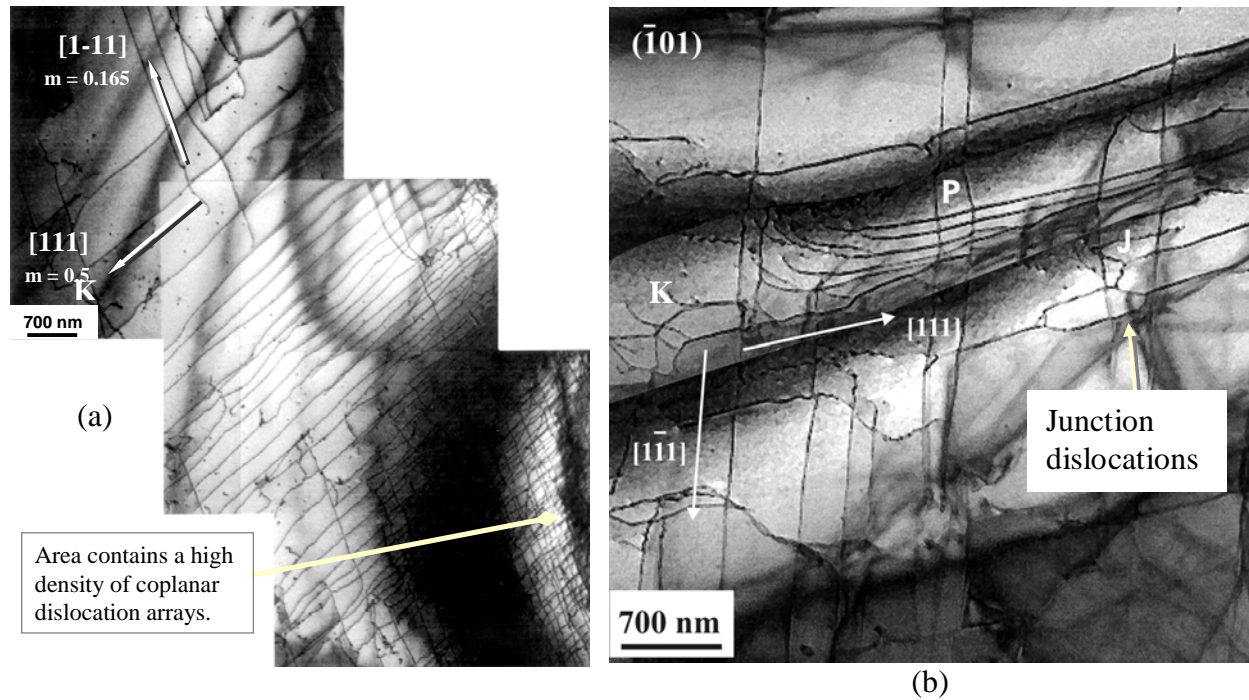

Fig. 13. Bright-field TEM images showing (a) a mutual trapping of the ±½[111] and ±½[1$\bar{1}$1] coplanar dislocation arrays on the ($\bar{1}$01) plane; (b) the formation of a pile-up array of ±½[111] screw dislocations at site **P** in front of junction dislocations at sites **J** and **K** on the ($\bar{1}$01) plane.

Proposed mechanisms for the anomalous slip

Based upon the TEM results shown above, the {0$\bar{1}$1} anomalous slip that occurred in the "single-slip" oriented sample deformed at room temperature can accordingly be rationalized by the collective effects of dislocation multiplication, interaction, and propagation, which include the simultaneous operations of primary and cooperative dislocation sources, the formation and interaction of coplanar dislocation arrays, the formation of junction dislocations, the formation of dislocation pile-ups, and the stress-induced cross slip of screw dislocations. The stress-induced cross-slip renders the propagation of ±½[111] screw dislocations from ($\bar{1}$01) onto (0$\bar{1}$1) and the propagation of ±½[1$\bar{1}$1] screw dislocation from ($\bar{1}$01) onto

(011), which subsequently activate the slip systems on the (0$\bar{1}$1) and (011) planes that are not allowed to operate according to the Schmid law.

Evidence showing the stress-induced cross slip of ±½[111] screw dislocations from the ($\bar{1}$01) plane onto the (0$\bar{1}$1) plane is demonstrated in Figure 14, in which multiple TEM images were taken from a sample sliced parallel to the (0$\bar{1}$1) plane. Here, a narrow ($\bar{1}$01) slip band, which is physically inclined to the (0$\bar{1}$1) plane at 60°, is seen in the lower portion to contain an array of ±½[111] dislocations traveling smoothly in the [111] direction; some zigzag-shaped pre-existing dislocation segments, presumably **b** = ±½[$\bar{1}$11], can also be found at the surrounding areas. An event of the stress-induced cross slip of ±½[111] screw dislocations can be readily seen in the upper portion of the slip band and the surrounding region specified by a white rectangular frame, in which some ±½[111] screw dislocations were observed to cross slip and propagate from the ($\bar{1}$01) slip band onto the (0$\bar{1}$1) plane as a result of the event of dislocation pile-up on the ($\bar{1}$01) plane as depicted in Figure 13. The cross-slip of ±½[111] screw dislocations in turn triggered the operations of the ±½[$\bar{1}$11] cooperative dislocation sources resulting from the interactions between the cross-slipped ±½[111] screw dislocations and the pre-existing ±½[$\bar{1}$11] dislocation segments and led to the formation of the ±½[111] and ±½[$\bar{1}$11] coplanar dislocation arrays on the (0$\bar{1}$1) plane. Figure 15a shows an image taken from an area adjacent to the cross-slip region shown in Figure 14, in which two long and straight ±½[111] screw dislocations are seen to move across an area of the (0$\bar{1}$1) plane containing many pre-existing ±½[$\bar{1}$11] dislocation segments (in a zigzag shape), meanwhile two long and straight ±½[$\bar{1}$11] screw dislocations, presumably formed by the operation of a cooperative source, are also seen to move across the same area.

Similarly, the ±½[1$\bar{1}$1] screw dislocations can also cross-slip from the ($\bar{1}$01) plane onto the (011) plane as a result of the mutual trapping of co-planar dislocation arrays and the dislocation pile-ups, which lead to the operations of the ±½[11$\bar{1}$] cooperative dislocation sources from the pre-existing ±½[11$\bar{1}$] dislocation

segments and result in the formation of the ±½[1$\bar{1}$1] and ±½[11$\bar{1}$] coplanar dislocation arrays on the (011)

plane as shown in Figure 15b. Here, several ±½[1$\bar{1}$1] screw dislocations are seen to move across an area of

the (011) plane, meanwhile, several long and straight ±½[11$\bar{1}$] screw dislocations are also seen to move

across the same area. The observations of mutual trapping of the ±½[111] and ±½[$\bar{1}$11] coplanar

dislocation arrays on the (0$\bar{1}$1) plane and mutual trapping of the ±½[1$\bar{1}$1] and ±½[11$\bar{1}$] coplanar dislocation

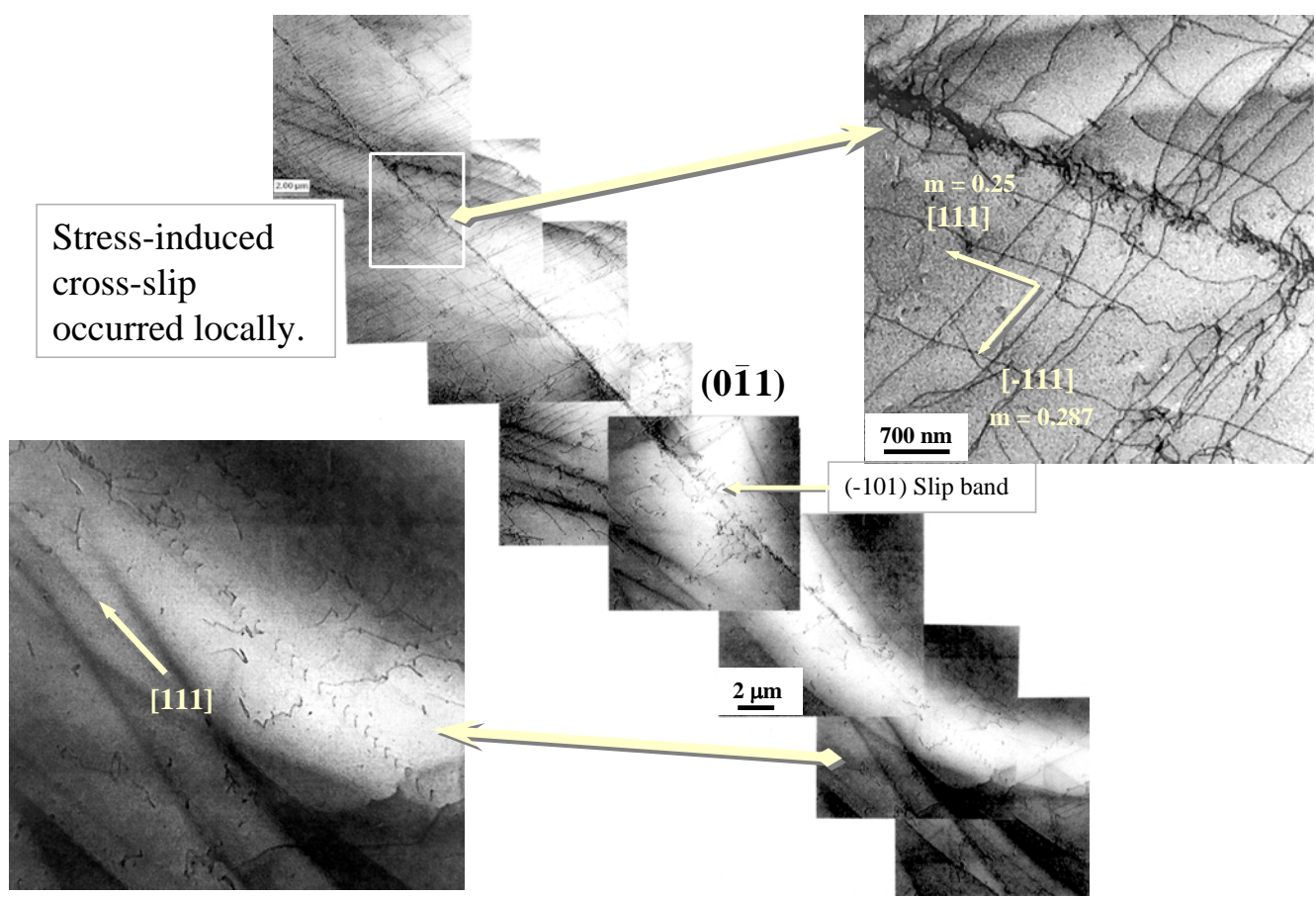arrays on the (011) plane are shown in Figures 16a and 16b, respectively.

Fig. 14. Bright-field TEM images showing the evidence of the stress-induced cross slip of ½[111] screw
dislocations from the local region of a ($\bar{1}$01) slip band onto the (0$\bar{1}$1) plane.
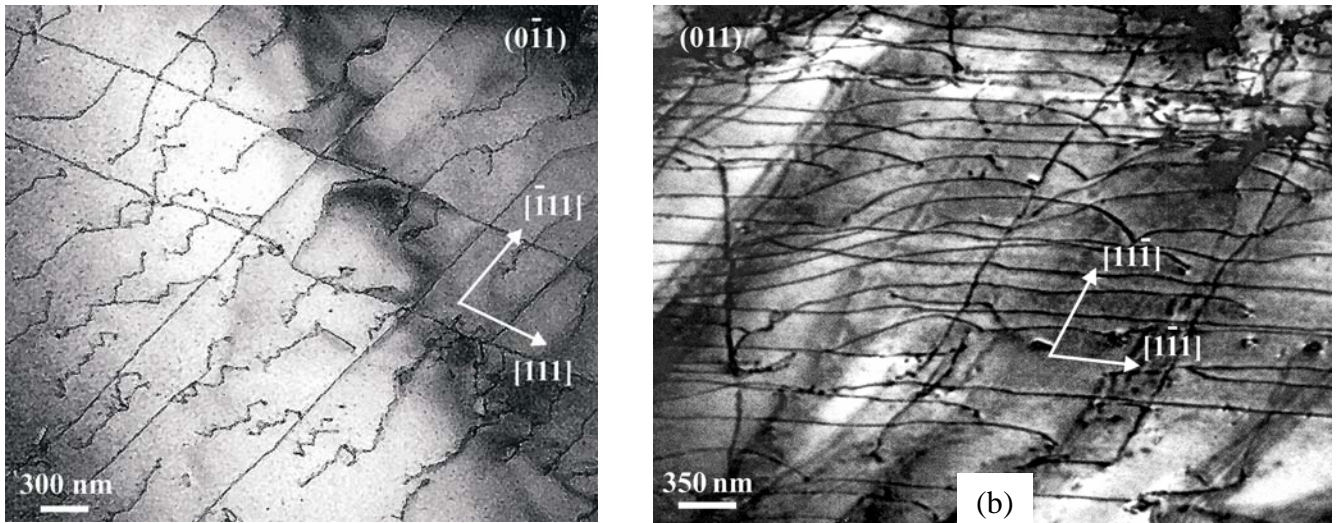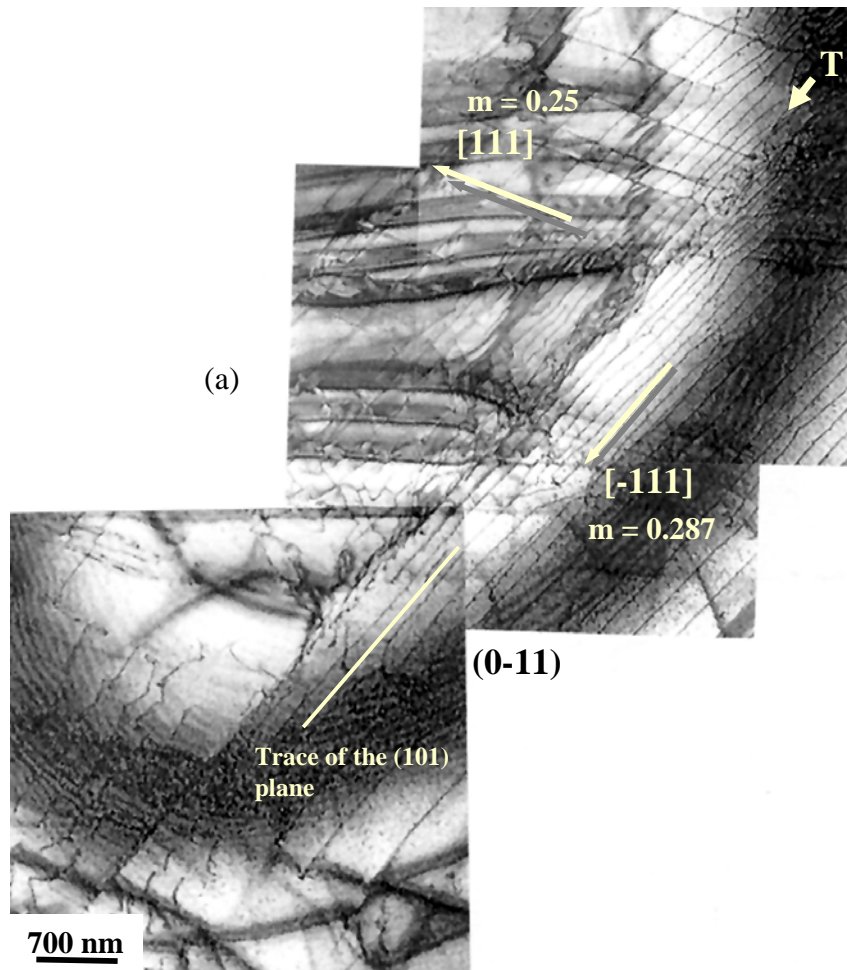
Fig. 15. Bright-field TEM images showing (a) the interaction between the cross-slipped ±½[111] screw dislocations and the pre-existing ±½[$\bar{1}$ 11] dislocation segments on the (0 $\bar{1}$ 1) plane, and (b) the formation of the ±½[1 $\bar{1}$ 1] and ±½[11 $\bar{1}$] coplanar dislocation arrays on the (011) plane.
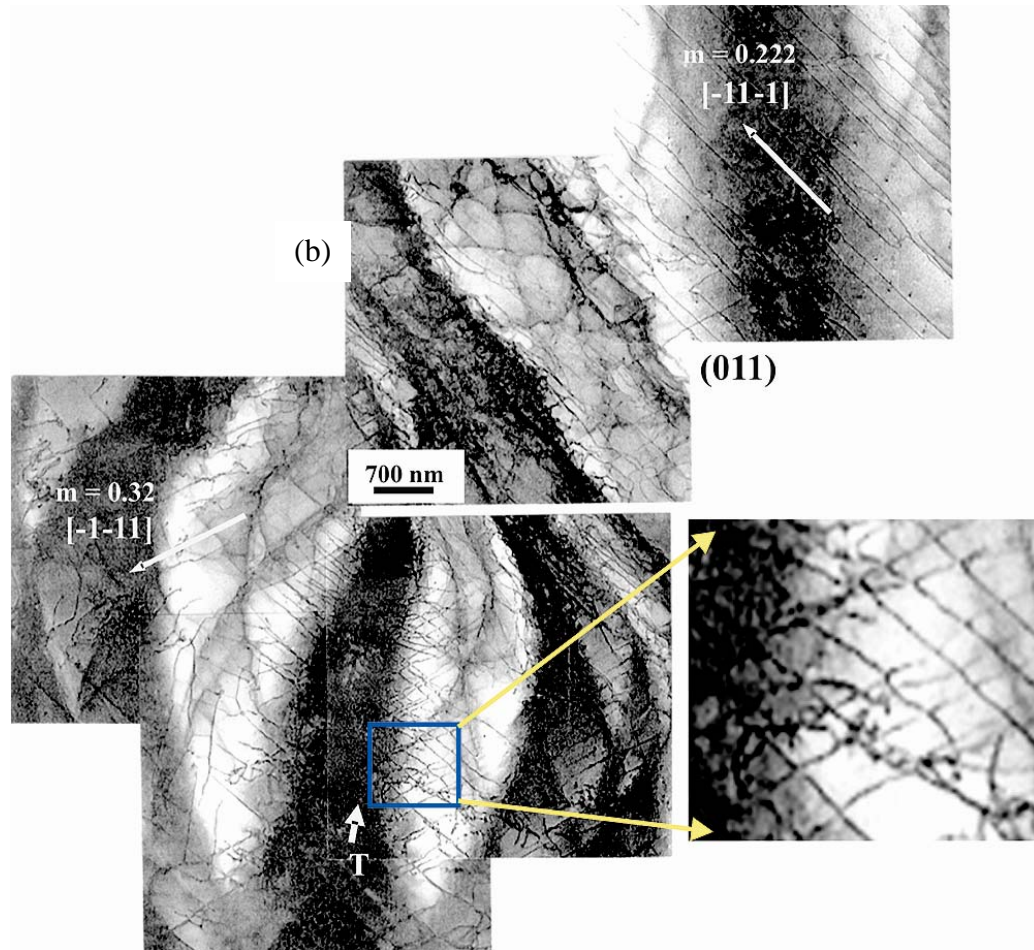
Fig. 16. Bright-field TEM images showing (a) mutual trapping of the $\pm\frac{1}{2}[111]$ and $\pm\frac{1}{2}[\bar{1}11]$ coplanar dislocation arrays (at site **T**) on the $(0\bar{1}1)$ plane, and (b) mutual trapping of the $\pm\frac{1}{2}[1\bar{1}1]$ and $\pm\frac{1}{2}[11\bar{1}]$ coplanar dislocation arrays and the formation of junction dislocations between the coplanar dislocation arrays (at site **T**) on the (011) plane.

Since the occurrence of anomalous slip is intimately related to the dynamic cross-slip of screw dislocations induced by local stress concentrations as a result of the mutual trapping and the dislocation pile-ups, it is suggested that the anomalous slip behavior of bcc metals is governed by the easiness of cross slip, which in turn is dependent on the strain rate and testing temperature. That is, when the cross slip of screw dislocations becomes prevalent under high-temperature and low strain-rate conditions, the mutual trapping and pile-ups of screw dislocations become less likely, and thus the anomalous slip phenomenon will be suppressed or vanished. Since collective effects of the cooperative dislocation multiplication, the

interaction between co-planar dislocation arrays, the mutual trapping and dislocation pile-ups can lead to the increase of not only the dislocation density but also the glide resistance for dislocation motion, it is anticipated that the work-hardening stage appears immediately after yielding.

Conclusion

The mysterious anomalous-slip phenomenon observed in bcc metals has been revisited and studied by conducting careful TEM examinations of the dislocation structures formed in the $[\bar{2}\ 9\ 20]$-oriented Mo single crystals compressed at room temperature to an axial strain of 0.6 % at a strain rate of 1 s^{-1}. The results reveal that the initial or "pre-existing" screw dislocations associated with "grown-in" jogs in as-annealed crystals can evolve and act as effective sources for multiplying both ±½[111] and ±½[1$\bar{1}$1] coplanar screw dislocation arrays on the ($\bar{1}$01) primary slip plane. The interaction between the ±½[111] primary dislocation arrays and the self-pinned ±½[1$\bar{1}$1] dislocation segments causes the operation of ±½[1$\bar{1}$1] dislocation sources, which subsequently results in the formation and motion of ±½[111] and ±½[1$\bar{1}$1] coplanar dislocation arrays on the ($\bar{1}$01) primary slip plane. The occurrence of {0$\bar{1}$1} anomalous slip can accordingly be attributed to the collective effects of dislocation multiplication, interaction, and propagation which include the simultaneous operations of primary and cooperative dislocation sources, the formation and interaction of coplanar dislocation arrays, the formation of junction dislocations, the formation of dislocation pile-ups, and the stress-induced cross slip of screw dislocations on the ($\bar{1}$01) slip plane. The stress-induced cross-slip renders render the propagation of both ±½[111] and ±½[1$\bar{1}$1] screw dislocations from the ($\bar{1}$01) plane onto the (0$\bar{1}$1) and (011) planes, which subsequently activate the slip systems on the (0$\bar{1}$1) and (011) planes that are not allowed to operate according to the Schmid law.

Acknowledgements

References

1. M. S. Duesberry and R.A. Foxall, Phil. Mag. **20** (1969), p. 710.

2. E. Schmid, Z. Elektrochem, **37** (1931), p. 447; E. Schmid and W. Boas, "Plasticity of Crystals," Hughes, London, 1950.

3. V. Vitek, Crystal Lattice Defects, **5** (1974), p.1.

4. C. Bolton and G. Taylor, Phil. Mag. **26** (1972), p. 1369.

5. F. Louchet and L. P. Kubin, Acta Metall. **23** (1973), p. 17.

6. A. J. Garratt-Reed and G. Taylor, Phil. Mag. **A39** (1979), p. 597.

7. J. W. Christian, Met. Tans. A, **14A** (1983), p. 1237.

8. W. Wasserbach, "Anomalous Slip in High-Purity Niobium and Tantalum Single Crystals," Pys. Stat. Sol. (a) **147** (1995), p. 417.

9. A. Seeger, Mater. Sci. and Eng., **A319-321** (2001), p.254.

10. J. P. Hirth and J. Lothe, *"Theory of Dislocations"*, 2nd ed., J. Wiley, New York, 1981.

11. D. H. Lassila, M. M. LeBlanc, and M. Rhee, Mat. Res. Soc. Symp. Proc. Vol. **779**, MRS (2003), W2.9.1.

12. F. C. Frank and W. T. Read, in *"Symposium on Plastic Deformation of Crystalline Solids,"* Carnegie Institute of Technology, Pittsburgh, 1950, p. 44.

13. A. Einstein, *"Investigations on the Theory of Brownian Movement,"* Methuen, London (1926), p. 9.

14. C. Frank, Physica, **15** (1949), p. 131.

15. J. D. Eshelby, F. C. Frank, and F. R. N. Nabarro, Phil. Mag. **42** (1951), p. 351.